New Interpretations of Measured Antihydrogen Velocities and Field Ionization Spectra

T. Pohl,[1] H. R. Sadeghpour,[1] and G. Gabrielse[2]

[1]*ITAMP, Harvard-Smithsonian Center for Astrophysics, Cambridge, Massachusetts 02138, USA*
[2]*Department of Physics, Harvard University, Cambridge, Massachusetts 02138, USA*

(Received 20 June 2006; published 5 October 2006)

We present extensive Monte Carlo simulations, showing that cold antihydrogen ($\bar{H}$) atoms are produced when antiprotons ($\bar{p}$) are gently heated in the side wells of a nested Penning trap. The observed $\bar{H}$ with high energies, that had seemed to indicate otherwise, are instead explained by a surprisingly effective charge-exchange mechanism. We shed light on the previously measured field-ionization spectrum, and reproduce both the characteristic low-field power law as well as the enhanced $\bar{H}$ production at higher fields. The latter feature is shown to arise from $\bar{H}$ atoms too deeply bound to be described as guiding center atoms, atoms with internally chaotic motion.

DOI: 10.1103/PhysRevLett.97.143401 PACS numbers: 36.10.−k, 34.70.+e, 52.20.Hv

The observation of cold antihydrogen by ATHENA [1] and ATRAP [2,3] ushered in a flurry of theoretical work [4–8] that aimed to better understand the properties of these atoms, and the conditions under which they would form and ionize in external fields. Nonetheless, no mechanisms for understanding two central features of subsequent measurements have emerged. First, ATRAP measured [9] a surprisingly high velocity for antihydrogen atoms traveling along the magnetic field direction (open circles in Fig. 1), despite a $\bar{H}$ production method in which $\bar{p}$ were given just enough energy to pass through a positron (e^+) plasma [3]. Second, ATRAP's field-ionization method [10] showed that the number of such atoms that survived an electric field F, parallel to the magnetic field B, decreases initially as F^{-2} (open circles in Fig. 2), for atoms appropriately described in the guiding center approximation (GCA) [11]. Also unexplained is a relatively enhanced production of more deeply bound $\bar{H}$ [10]. Both unexplained features have important implications for the long term goal to trap ground state $\bar{H}$ for spectroscopy [12]. Enhanced production of $\bar{H}$ atoms closer to the desired ground state is good, while higher $\bar{H}$ velocities hurt prospects for $\bar{H}$ trapping in the very shallow traps that can be constructed.

In this Letter, we propose that the observed high $\bar{H}$ velocities arise from charge exchange of low-energy $\bar{H}$ atoms with fast $\bar{p}$ in the side wells of the nested Penning trap. Using simulations, we demonstrate that this process occurs with large probability, implying that initially formed $\bar{H}$ atoms are much slower than observed. The simulations reproduce both the observed low-field-ionization spectrum and the enhanced production of more deeply bound states. Based on the GCA, we can explain the observed F^{-2} spectrum for low ionization field within a simple, intuitive two-step model. The enhanced production of deeply bound $\bar{H}$, on the other hand, is found to be linked to the increasingly chaotic internal $\bar{H}$ motion, such that the GCA and the assumption of infinite $\bar{p}$ mass break down.

The high rate mechanism for producing cold $\bar{H}$ atoms in a nested Penning trap is three-body capture of e^+ by $\bar{p}$ in which a second e^+ is needed to conserve energy and momentum [13,14]. Early $B \to \infty$ calculation [11] revealed that the $\bar{H}$ formation rate scales with e^+ density (n_e) and temperature (T_e), as $n_e^2 T_e^{-9/2}$. They also showed the importance of replacement collisions, in which a bound e^+ was replaced by a e^+ trapped in an orbit closer to the $\bar{p}$, and the likelihood of producing GCA atoms with regular internal orbits. Simulations after the observations of slow

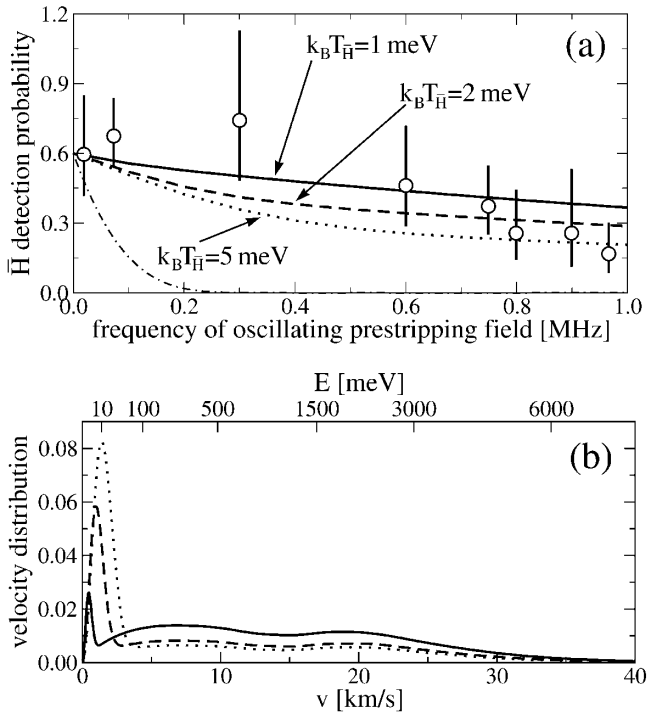

FIG. 1. Charge exchange produces the observed frequency-dependent field-ionization spectrum [9] (○). The spectra have been calculated for $k_B T_{\bar{p}} = 8$ eV. The dot-dashed line shows the spectrum that results by neglecting e^+ charge transfer for $kT_{\bar{H}} = 2$ meV ($T_{\bar{H}} = 30$ K). (b) Corresponding velocity distributions after charge exchange. See text for details.

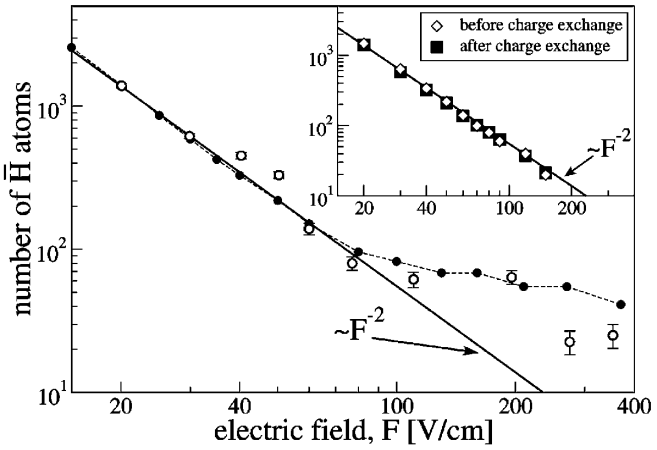

FIG. 2. Field-ionization spectrum of $\bar{H}$ atoms that survive an electric field F. ATRAP measurements [10] (○) are compared to exact Monte Carlo calculations for $kT_{\bar{H}} = 2$ meV (●) of $\bar{H}$ produced by TBC. The inset demonstrates that charge exchange does not alter the field-ionization spectrum by comparing the GCA simulations before (◇) and after (■) charge exchange. The theoretical curves have been rescaled to match the measured atom number at 20 V/cm.

$\bar{H}$ atoms also included $\bar{p}$ motional effects [4] and approximation of experimental geometries [7] and non-GCA effects [5,6,10]. However, no understanding of either the field ionization or the higher than expected $\bar{H}$ velocities emerged.

Here we propose solutions to these outstanding questions and verify them with classical Monte Carlo simulations. As is appropriate for low $\bar{p}$ number and high e^+ density, we neglect the $\bar{p}$-$\bar{p}$ interaction and calculate the classical dynamics of a single $\bar{p}$ traveling through the e^+ plasma, as in [4,11]. Since collective excitations do not significantly affect the recombination process, only the e^+ dynamics in a finite cubic box centered around a moving $\bar{p}$ is considered. The e^+ are randomly injected into the box according to a phase space distribution at the temperature T_{e^+}. The launching of e^+ stops as soon as the $\bar{p}$ has traveled long enough to escape the e^+ cloud, after which we slowly ramp-up the electric field to determine the value F at which the $\bar{H}$ ionizes.

Because of disparate time scales in the cyclotron, magnetron, and axial motions, serious numerical challenges require a two-tier numerical strategy. First, a straightforward GCA calculation freezes out the e^+ cyclotron motion [4]. Second, a full numerical simulation relies on a symplectic integrator [5] but with a time-coordinate transformation and improved partitioning of the Hamiltonian [15]. These computational advances allow us to describe the long-time dynamics of very deeply bound atoms (e.g., Fig. 3), and also to investigate the range of validity of the GCA.

The field-ionization spectrum from the exact calculation compares well to experimental observations [10] (Fig. 2). The GCA reproduces the observed F^{-2} dependence at low F, but deviates significantly from the observations at large F. (The implications for the field-ionization spectrum due to charge-exchange are discussed later in the text.) The simulations show that atoms form in a two-step process. A e^+ is initially captured at the edge of the kinetic bottleneck [binding energy of a few $k_B T_{e^+}$ below which reionization is suppressed [11]] and subsequently driven down in a *single* deexciting collision.

This two-step process allows us to derive the observed low-field F^{-2} behavior within the GCA. After the initial step, the GCA atoms formed near the bottleneck and in thermal equilibrium with the surrounding $\bar{p}$ plasma, have energies E_i with densities per unit energy $W_{\rm eq}(E_i)$. The one-way collisional rate of transitions out of equilibrium to a final energy E_f below the bottleneck is proportional to $R(E_f, E_i) \propto n_{\bar{p}} n_{e^+}^2 e^{-\varepsilon_i} (-E_f)^{-\varepsilon_b}$ [Eq. III.11, Ref. [14]]. Here $n_{\bar{p}}$ is the $\bar{p}$ density, and ε_i and $\varepsilon_b - 1$ are the initial and bottleneck energies in units of $k_B T_{e^+}$. The value of ε_b for the field-free [14] and infinite-field [11] cases is $\epsilon_b \sim 5$. The collisional deexcitation rate constant is expressed as $K(E_f, E_i) = R(E_f, E_i)/[W_{\rm eq}(E_i) n_{e^+}]$ [Eq. III.10, Ref. [14]].

The dependence of this rate constant on the final energy of the eventually detected atoms is given by $K(E_f, E_i) \propto (-E_f)^{-\epsilon_b}$, such that their binding energy distribution is

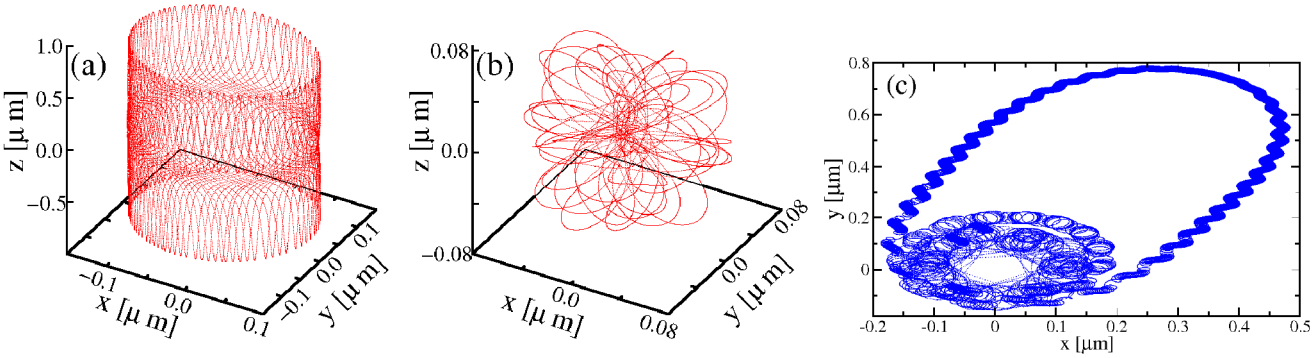

FIG. 3 (color online). Typical e^+ example of a small-ρ GCA atom (a), a small-ρ non-GCA atom (b), and an intermittent chaotic trajectory (c). z is along the B field axis, and $\rho = [x^2 + y^2]^{1/2}$ is the transverse coordinate.

$P(E)dE \sim K(E, E_i)dE \sim E^{-\epsilon_b}dE$. The minimum ionization field and binding energy of GCA atoms scale, respectively, as $F \sim \rho/(\rho^2 + z_m^2)^{3/2}$ [6] and $E \propto 1/\sqrt{\rho^2 + z_m^2}$, where z_m denotes the amplitude of the axial bounce motion—for $z_m < \rho$, the radius at which an $\bar{H}$ atom ionizes scales as $F^{-1/2}$ [6]. Upon a coordinate transformation [16], we obtain the ionization field distribution $P(F)dF = F^{-[(\varepsilon_b+1)/2]}dF$. Thus, the total number of atoms surviving a given ionization field is $N_F \propto \int_F^\infty \tilde{F}^{-[(\varepsilon_b+1)/2]}d\tilde{F} \sim F^{-2}$.

For more deeply bound atoms, the complete simulation reveals intermittent chaos [16] that the GCA cannot describe. The e^+ undergoes chaotic motion while trapped close to the $\bar{p}$, interrupted by elliptical e^+ excursions [see Fig. 3(c)]. Importantly, the GCA and non-GCA atoms formed with small transverse sizes are quite different. In the GCA case, we find that small-ρ atoms are typically elongated in the axial direction [Fig. 3(a)]. Within our exact calculations, the strong coupling between the cyclotron, magnetron and axial motions fills a nearly spherical volume in phase space, leading to tightly bound and nearly spherical states [Fig. 3(b)], which survive large ionization fields. The net result is a departure from the F^{-2} behavior, shown in Fig. 2 and observed in the measurement. As previously anticipated [10], there is now convincing evidence in theory that ATRAP has detected $\bar{H}$ atoms too deeply bound to be described by the GCA.

Thus far, we assumed low axial kinetic $\bar{p}$ energies of a few meV, as might be expected from gently heating the $\bar{p}$ in the side wells of the nested trap until they have just enough energy to pass through the e^+ plasma [3,9]. This, however, is in marked contrast to the observed oscillating-field spectrum, which is consistent with a monoenergetic velocity distribution of 200 meV [9] (Fig. 1). We propose instead a new interpretation—that low energy $\bar{H}$ are produced, and subsequent charge exchange with fast $\bar{p}$ in the side wells of the nested Penning trap yields the high velocity atoms that were observed.

Could the fractional probability for charge-exchange of slow Rydberg $\bar{H}$ atoms with fast $\bar{p}$ ions in a magnetic field be large? In the field-free hydrogen-proton charge-exchange collision, the cross section increases as n^4, where n is the principal quantum number of the target state [18]. For large B, where n is no longer a good quantum number, calculations are scarce. There is one example [18], in which extremely large capture cross sections, $\sim 10^{-10}$ cm^2, were predicted for Rydberg electron capture from an $n = 28$ state in a $B = 4$ T field. Scaling to Rydberg states near $n = 100$ gives a cross section that is at least 2 orders of magnitude larger. A microcanonical distribution of an infinitely massive atom for the initial target states was assumed in [18]. Here, we instead calculate the charge-exchange cross section for each microscopic internal and translational atomic state as produced by our preceding simulation of the capture process. The initial and final states of the $\bar{H}$ atoms are classified by the maximum fields, F_i and F_f, that they survive. By averaging over F_f and all charge-exchanged $\bar{H}$ atoms for a given F_i, we obtain the average total capture cross section $\bar{\sigma}_{cx}(F_i; v_{\bar{H}}, v_{\bar{p}})$ as a function of the initial $\bar{H}$ velocity $v_{\bar{H}}$ and the $\bar{p}$ (projectile) velocity $v_{\bar{p}}$.

Figure 4(a) shows the extremely large charge exchange cross sections as a function of the $\bar{p}$ energy for 20 V/cm $\leq F_i \leq$ 60 V/cm. The inset shows $\bar{\sigma}_{cx}$ in units of πa_0^2, where a_0 is the Bohr radius, as a function of the relative collision velocity scaled by the average axial positron velocity $\bar{v}_z = \sqrt{\langle v_z^2 \rangle}$ of the target $\bar{H}$. Pronounced "humps" in the cross sections occur when the Rydberg e^+ and $\bar{p}$ velocities match [17].

For a given $n_{\bar{p}}$ and $\bar{p}$ cloud size (d), the corresponding capture probability is obtained from

$$\bar{P}_{cx}(F; v_{\bar{p}}, v_{\bar{H}}) = 1 - e^{-\bar{\sigma}_{cx} n_{\bar{p}} d(v_{\bar{p}}/v_{\bar{H}})}, \quad (1)$$

to be compared to the fraction of detectable slow $\bar{H}$ atoms $\kappa(1 - \bar{P}_{cx})$. The $\bar{H}$ travel time through the $\bar{p}$ cloud is $d/v_{\bar{H}}$. The velocity dependent detection efficiency $\kappa(v_{\bar{H}})$ is calculated by assuming transverse thermal diffusion at 4.2 K and a detection solid angle of $2\pi/100$ [3]. As shown in Fig. 4(b), for a typical $v_{\bar{H}}$, a considerable fraction $\bar{P}_{cx}/[\bar{P}_{cx} + \kappa(1 - \bar{P}_{cx})]$ of $\bar{H}$ atoms are fast atoms produced in charge exchange.

The average charge-exchange probability is almost independent of the target $\bar{H}$ ionization field [Fig. 4(b)]. Additionally, the charge exchange broadens the final ion-

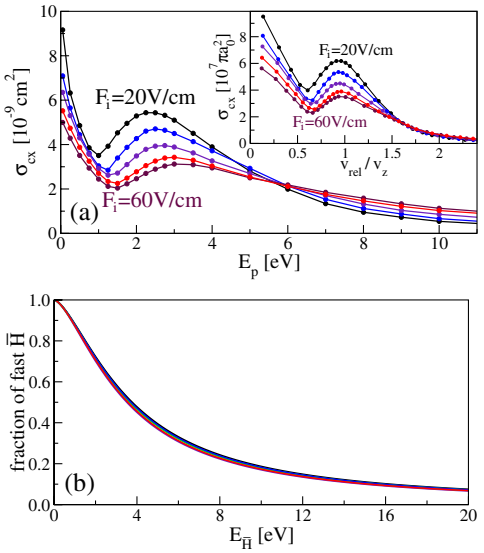

FIG. 4 (color online). (a) e^+ exchange cross section from 1 meV $\bar{H}$ atoms as a function of $\bar{p}$ axial energy, for different ionization fields in the range, 20–60 V/cm, with increasing values of F_i from top to bottom. The inset shows the cross sections in units of πa_0^2 as a function of the relative $\bar{p}$-$\bar{H}$ velocity scaled by the average axial e^+ velocity of the atomic target state. (b) Corresponding fraction of fast $\bar{H}$ atoms as a function of the kinetic energy of the slow target (TBC) atoms and a projectile $\bar{p}$ temperature in the side wells of $k_B T_{\bar{p}} = 8$ eV.

ization field distribution with an average field value $\langle F_f \rangle$ close to the initial field F_i. Together, these observations yield a field-ionization spectrum which remains unaltered by the charge-exchange collisions (inset of Fig. 2), where we compare the GCA field-ionization spectrum before and after charge exchange in the side wells, calculated from the final-state resolved charge-exchange cross sections.

The final distribution $\phi(v)$ of axial $\bar{H}$ velocities is obtained by adding the contributions from the fast (slow) atoms that do (do not) charge exchange,

$$\phi(v) = \int [1 - \bar{P}_{cx}(v_{\bar{p}}, v)]\kappa(v)\phi_{\bar{H}}(v)\phi_{\bar{p}}(v_{\bar{p}})dv_{\bar{p}} + \int \bar{P}_{cx}(v, v_{\bar{H}})\phi_{\bar{H}}(v_{\bar{H}})\phi_{\bar{p}}(v)dv_{\bar{H}}. \quad (2)$$

Here, $\phi_{\bar{H}}$ and $\phi_{\bar{p}}$ denote the axial velocity distributions of the slow initially formed $\bar{H}$ atoms and the fast $\bar{p}$ ions, both assumed to be Gaussian with thermal spreads of $T_{\bar{H}}$ and $T_{\bar{p}}$, respectively. While the $\bar{p}$ axial velocity distribution is unknown, the $\bar{p}$ velocity spread is roughly the side well depth—about 10 eV for ATRAP. Since the charge-exchange cross section quickly drops for $\bar{p}$ energies larger than 2 eV, the final $\bar{H}$ velocity distribution is found to be nearly independent of $\bar{p}$ axial energy spread in the typical range of 3–15 eV, and hence also independent of the exact shape of $\phi_{\bar{p}}$. From Eq. (2), we calculate the final $\bar{H}$ velocity distribution for initial average energies ranging from 1 meV to 10 meV, some of which are illustrated in Fig. 1(b). The pronounced peak at small velocities corresponds to the slow atoms that do not charge exchange, reflecting $\varphi_{\bar{H}}$. The extended plateau at much higher velocities, independent of $\varphi_{\bar{H}}$ and $\varphi_{\bar{p}}$, arises from charge exchange with the fast $\bar{p}$ in the side wells.

The calculated field-ionization spectra (Fig. 1) agree with the experimental data for $\bar{H}$ velocity spreads of $k_B T_{\bar{H}} = 1$ meV to $k_B T_{\bar{H}} = 10$ meV, as well as does a 200 meV monoenergetic $\bar{H}$ beam [9]. The charge-exchange mechanism provides an alternative and self-consistent interpretation of the measurements, whereby a significant fraction of $\bar{H}$ atoms become fast atoms, while others that do not undergo charge exchange acquire little velocity. Without charge exchange, the resulting velocity spectrum does not agree with the experiment [dot-dashed line in Fig. 1(a)].

Our analysis may apply to the case of high energy $\bar{p}$ slowed by e^+ to form $\bar{H}$, as in the first ATRAP observation [2] and all of the ATHENA observations [1,19], if the e^+ cooling of the $\bar{p}$ is sufficiently efficient, but no explicit calculation has been performed here for this situation. Moreover, fast charge exchanged $\bar{H}$ may not have been observed in the ATHENA apparatus, which detects $\bar{H}$ atoms traveling transversally to B.

In conclusion, we have demonstrated that charge-exchange collisions are likely responsible for the higher-than-thermal velocities that ATRAP observed for $\bar{H}$ produced during the e^+ cooling of $\bar{p}$ in a nested Penning trap, even when the $\bar{p}$ are just given enough energy to pass through the e^+ plasma. The important implication for the experiments is that much slower $\bar{H}$ atoms are being produced than might be inferred from the observed velocity spectrum, some being slow enough to be trapped. ATRAP's measured field ionization spectrum is theoretically reproduced for the first time. The observed low-field F^{-2} behavior indicates that $\bar{H}$ are preferentially formed in a two-step process, rather than by multiple collisions below the kinetic bottleneck. Our exact classical Monte Carlo simulations have revealed a breakdown of the guiding center approximation at high ionization fields, i.e., deep atomic binding energies. Whereas the guiding center calculations follow the F^{-2} over the range of electric fields, the exact dynamics reproduces the experimentally observed relative enhanced production of deeply bound, non-GCA atoms. Radiative decay may be more efficient because of the rapid acceleration of chaotic atoms.

This work was partially supported by NSF through a grant for ITAMP.

[1] M. Amoretti *et al.*, Nature **419**, 456 (2002).
[2] G. Gabrielse *et al.*, Phys. Rev. Lett. **89**, 213401 (2002).
[3] G. Gabrielse *et al.*, Phys. Rev. Lett. **89**, 233401 (2002).
[4] F. Robicheaux and J. D. Hanson, Phys. Rev. A **69**, 010701(R) (2004).
[5] S. X. Hu, D. Vrinceanu, S. Mazevet, and L. A. Collins, Phys. Rev. Lett. **95**, 163402 (2005).
[6] D. Vrinceanu *et al.*, Phys. Rev. Lett. **92**, 133402 (2004).
[7] F. Robicheaux, Phys. Rev. A **70**, 022510 (2004).
[8] S. G. Kuzmin and T. M. O'Neil, Phys. Plas. **12**, 012101 (2005).
[9] G. Gabrielse *et al.*, Phys. Rev. Lett. **93**, 073401 (2004).
[10] G. Gabrielse, Adv. At. Mol. Opt. Phys. **50**, 155 (2005).
[11] M. Glinsky and T. O'Neil, Phys. Fluids B **3**, 1279 (1991).
[12] G. Gabrielse, in *Fundamental Symmetries*, edited by P. Bloch, P. Paulopoulos, and R. Klapisch (Plenum, New York, 1987), pp. 59–75.
[13] G. Gabrielse, S. L. Rolston, L. Haarsma, and W. Kells, Phys. Lett. A **129**, 38 (1988).
[14] P. Mansbach and J. Keck, Phys. Rev. **181**, 275 (1969).
[15] T. Pohl and H. R. Sadeghpour (to be published).
[16] P. Schmelcher and L. S. Cederbaum, Phys. Rev. A **47**, 2634 (1993).
[17] D. M. Homan *et al.*, Phys. Rev. A **58**, 4565 (1998); K. B. MacAdam *et al.*, Phys. Rev. Lett. **75**, 1723 (1995); V. N. Ostrovsky, J. Phys. B **28**, 3901 (1995).
[18] S. Bradenbrink *et al.*, J. Phys. B **30**, L161 (1997).
[19] N. Madsen *et al.*, Phys. Rev. Lett. **94**, 033403 (2005).